Supporting Information

Li et al. 10.1073/pnas.1713905115

SI Text

Uncertainty Analysis for Calcium Wave Speed Calculation. The reading error in measuring the small-region position (e_{rp}) is determined by the resolution of our imaging system and related to the percent uncertainty (u_{x_i} and u_{y_i}) in measuring the coordinates of the centers (x_i and y_i) of small regions (circle or rectangular) through

$$e_{rp} = x_i \cdot u_{x_i} = y_i \cdot u_{y_i} \ (i = 1, 2, 3, 4, 5, 6). \quad \text{[S1]}$$

In combination with Eq. **S1**, the percent uncertainty in distance calculation is given by

$$u_{d_{ij}} = \sqrt{\left(\frac{x_i}{d_{ij}} \cdot \frac{\partial d_{ij}}{\partial x_i} \cdot u_{x_i}\right)^2 + \left(\frac{x_j}{d_{ij}} \cdot \frac{\partial d_{ij}}{\partial x_j} \cdot u_{x_j}\right)^2 + \left(\frac{y_i}{d_{ij}} \cdot \frac{\partial d_{ij}}{\partial y_i} \cdot u_{y_i}\right)^2 + \left(\frac{y_j}{d_{ij}} \cdot \frac{\partial d_{ij}}{\partial y_j} \cdot u_{y_j}\right)^2}, \quad \text{[S2]}$$

$$(i = 1, 2, 3 \ and \ j = i + 3)$$

where

$$\frac{\partial d_{ij}}{\partial x_i} = \frac{\partial\left[\sqrt{(x_i - x_j)^2 + (y_i - y_j)^2}\right]}{\partial x_i} = \frac{x_i - x_j}{d_{ij}} \quad \text{[S3]}$$

$$\frac{\partial d_{ij}}{\partial y_i} = \frac{\partial\left[\sqrt{(x_i - x_j)^2 + (y_i - y_j)^2}\right]}{\partial y_i} = \frac{y_i - y_j}{d_{ij}}. \quad \text{[S4]}$$

Further, Eq. **S2** can be simplified to

$$u_{d_{ij}} = \frac{e_{rp}}{d_{ij}} \sqrt{\frac{2(x_i - x_j)^2 + 2(y_i - y_j)^2}{{d_{ij}}^2}} = \sqrt{2} \cdot \frac{e_{rp}}{d_{ij}}. \quad \text{[S5]}$$

The error in measuring the 50% risetime difference between region i and region j (e_{td}) depends on the collection time interval of our imaging system and raw data postprocessing through

$$e_{td} = t_i \cdot u_{t_i} \ (i = 1, 2, 3, 4, 5, 6). \quad \text{[S6]}$$

Similarly, the percent uncertainty in calculating the time difference is

$$u_{t_{ij}} = \sqrt{\left(\frac{t_j}{t_{ij}} \cdot \frac{\partial t_{ij}}{\partial t_j} \cdot u_{t_j}\right)^2 + \left(\frac{t_i}{t_{ij}} \cdot \frac{\partial t_{ij}}{\partial t_i} \cdot u_{t_i}\right)^2}, \quad \text{[S7]}$$

where $t_{ij} = t_j - t_i$, and t_i and t_j are the risetime to 50% peak value of calcium concentration change for regions i and j, respectively. Eq. **S7** can be simplified to

$$u_{t_{ij}} = \sqrt{2} \cdot \frac{e_{td}}{t_{ij}}. \quad \text{[S8]}$$

Finally, the percent uncertainty in calculating the calcium wave speed can be derived as

$$u_{C_{ij}} = \sqrt{(u_{d_{ij}})^2 + (u_{t_{ij}})^2}. \quad \text{[S9]}$$

From Eqs. **S5**, **S8**, and **S9**, it can be seen that, for calcium waves propagating through cells of the same dimension, the uncertainty in calcium wave speed calculation is larger for cells with higher calcium wave speed. Based on the experimental data collected from the FL recordings, the average uncertainties in the calcium wave speed calculation were estimated to be 36%, 11%, and 5% at S_d = 30, 40, and 50 μm, respectively.

Immunofluorescent Staining. Standard immunofluorescence procedures (59) were slightly modified to treat the patterned HeLa cells in the microfluidic channels. All media were initially injected into the channel at a flow rate of 10 μL/min for ∼1 min, and then adjusted to and sustained at 1 μL/min for varying incubation times. First, cells were incubated for 15 min in 4% paraformaldehyde (Sigma P6148) at the end of experiments to fix their cytoskeletal structures. Afterward, 10 mM NH_4Cl (Sigma A9434) in PBS was applied for 15 min to quench the fixative. Cell membranes were then permeabilized through a 15-min application of 0.1% TritonX-100 (Sigma T8787) in PBS, after which the cells were washed with 0.05% Tween-20 (Sigma P2287) in PBS. Actin staining was accomplished by incubating cells for 15 min with 1% phalloidin conjugated Alexa Fluor 488 (Thermo A12379) in PBS. Afterward, cells were cured in ProLong Diamond Antifade Mountant with DAPI (Thermo P36961) overnight. The PBS solutions aforementioned are 1× PBS.

Confocal Imaging. Microfluidic chips were mounted on a motorized stage and imaged with a 100× oil objective on a Leica SP5 inverted confocal microscope, in which the 405-nm Diode, 488-nm Argon lasers were used in two separate channels to collect blue (DAPI) and green (Alex Fluor 488) FL. Gain and power of the lasers were adjusted for the first cell imaged in each microfluidic chip, and were held constant for all images taken subsequently from the same chip. Z-stacks were taken at the optimized setting and combined into maximum intensity projections using the Leica microscope software.

Stress Fiber Count. Stress fibers were identified manually from raw image data, based on a set of criteria described in a previous study (60). First, because stress fibers are stretched filaments under tension, they must be straight without buckling or sharp-angled turns. Some stress fibers may be slightly curved by being bound to other structures somewhere between their two ends. Second, stress fibers contain high actin content and therefore must appear to meet some minimum intensity value. Structures below the average intensity value of the entire cell were not included as stress fibers. Some cells exhibited a high degree of cytosolic noise, making it difficult to determine stress fibers from other actin structures. Those cells were excluded from further stress fiber analysis.

Single-Bubble Study with Beads and Ion Channel Inhibitors. To further confirm the binding specificity of beads-enhanced Ca^{2+} response observed in the TB experiments (Fig. 6*D*), we performed additional experiments using single-bubble (D_{max} = 51 ± 5 μm) treatment at S_d = 40 μm (Fig. S5*A*). The results showed that no intracellular Ca^{2+} response could be elicited without bead attachment.

Similarly, no enhancement of the Ca^{2+} response was observed with 6-μm BSA beads that were nonspecifically bound to the cell membrane. In contrast, the Ca^{2+} response probability was increased to 66.7% with 6-μm RGD beads through integrin binding; see Fig. S5*B*. This enhanced response at S_d = 40 μm was significantly inhibited by pretreatment with blockers of mechanosensitive ion channels, including either Gd^{3+} (100 μM) or RR (30 μM); see Fig. S5*C*. Altogether, these results suggest that stress–integrin signal transduction pathway and mechanically gated channels [e.g., TRPM7, as reported in HeLa cells whose function can be blocked by both Gd^{3+} and RR (41)] are responsible for the observed findings.

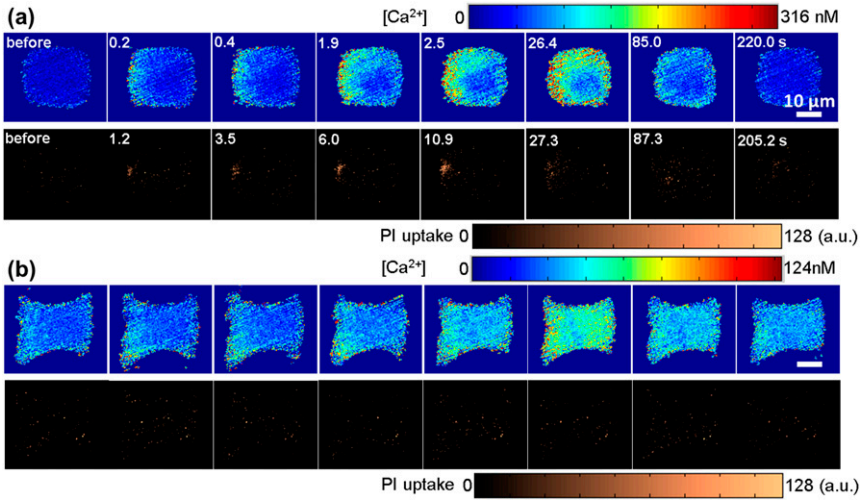

Fig. S1. FL image sequences of $[Ca^{2+}]_i$ variation (Top Row) and PI uptake (Bottom Row) in the cell shown in (*A*) Fig. 2*C* and (*B*) Fig. 2*D*. The color bars have been rescaled to show more clearly the changes in $[Ca^{2+}]_i$ and PI uptake. The timing for the image sequences are the same for *A* and *B*.

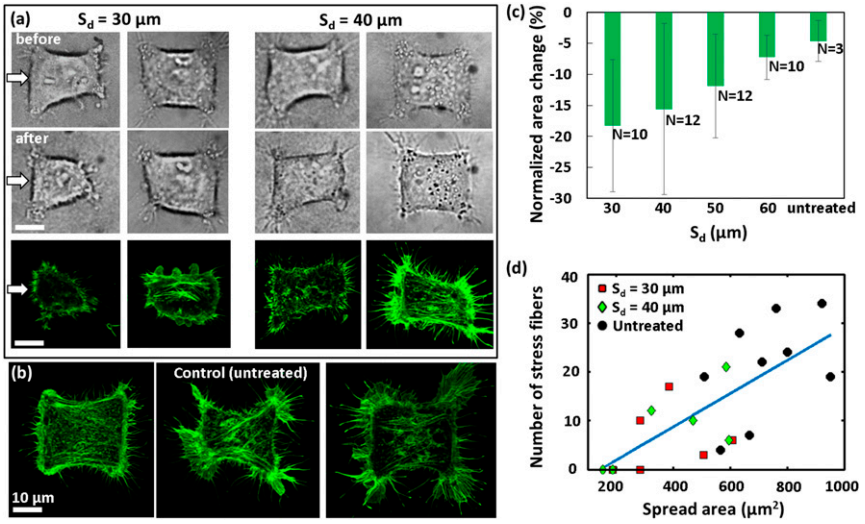

Fig. S2. (*A*) Examples of the BF images of two individual cells (*Top*) before and (*Middle*) after TB treatment at S_d = 30 and 40 μm, and (*Bottom*) confocal images of the cell's cytoskeleton with stress fiber staining (cells fixed at 2 h after the TB treatment). The cells in the S_d = 30 μm group show significant area reduction or blebbing indicating cell apoptosis. (*B*) Cytoskeleton images of untreated cells, which show more stress fibers. (*C*) Reduction of cell spread area after TB treatment (measured based on BF images), which was found to correlate negatively with S_d. (*D*) Number of stress fibers vs. spread area of individual cells (measured from confocal images) with or without TB treatment; the cells treated at S_d = 30, 40 μm (with membrane poration) show less stress fibers compared with the untreated group. (Scale bars, 10 μm.)

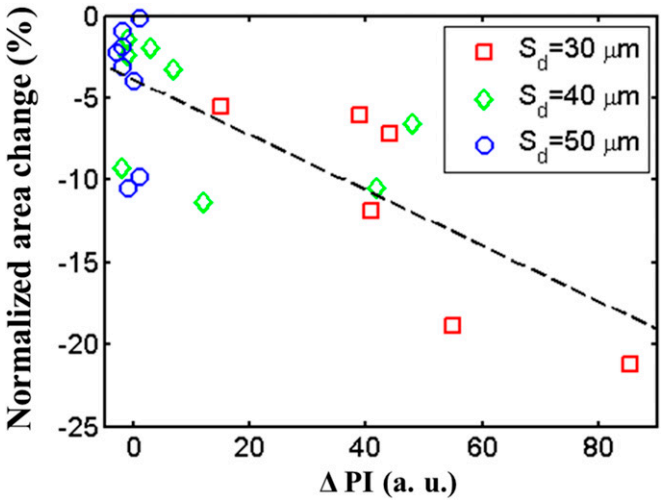

Fig. S3. Relationship between normalized spreading area change and PI uptake in individual cells treated by TB at $S_d = 30$, 40, and 50 μm. Note that spreading area changes were determined based on BF images taken before and after the TB treatment. The data indicate that the reduction in cell spreading area generally correlated with the amount of PI uptake, which indicates the severity of membrane poration and cell injury.

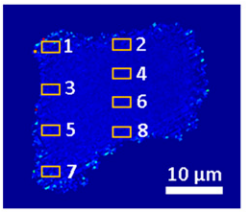

Speed ($\mu m/s$)	1->2 (edge)	7->8 (edge)	3->4 (inside)	5->6 (inside)	Ratio (edge/ inside)
Cell #1	107.82	79.70	34.50	42.80	2.43
#2	54.71	96.25	53.75	40.53	2.04
#3	24.08	67.53	32.81	18.40	2.64
#4	50.78	102.23	36.09	46.51	2.48

Fig. S4. Comparison of intracellular calcium wave speed near the edge to inside the cell. (*Left*) A representative cell (#4 in this figure, also shown in Fig. 4) with labeled small regions used for wave speed calculations. (*Right*) A table summarizing the calculation results of the wave speed, and the ratio of wave speed at cell edge [average of the number(s) underlined] to that inside the cell (average of the two measurements) from four individual cells treated at either $S_d = 30$ μm (cells #1, 2, and 3) or 40 μm (cell #4). These results provide preliminary evidence supporting the possibility of ICW propagation via CICI mechanism in the relatively thin and flat peripheral region of the cell.

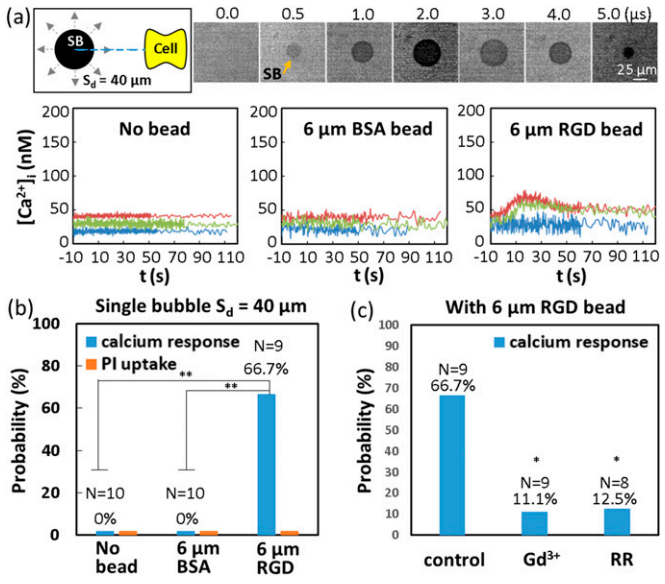

Fig. S5. HeLa cells treated with single bubble (SB) with a maximum diameter $D_{max} = 51 \pm 5$ μm at $S_d = 40$ μm. (*A*) Schematic diagram of the (*Top Left*) SB–cell interaction, (*Top Right*) SB dynamics, and (*Bottom*) three representative Ca^{2+} response profiles for cells with no bead, attached with 6-μm BSA beads, and attached with 6-μm RGD beads. (*B*) Probability of Ca^{2+} response (blue bar) and PI uptake (orange bar) for cells with no beads, attached with 6-μm BSA beads and 6-μm RGD beads. (*C*) Probability of Ca^{2+} response for cells attached with 6-μm RGD beads: control, pretreated with ion channel inhibitor Gd^{3+} (100 μM), or RR (30 μM) in PBS. Only individual cells with beads attached on the leading edge were selected for single-bubble treatment. $^{**}P < 0.01$; $^{*}P < 0.05$.

Table S1. Illustration of the calculation processes and results of C_{ICW} for cell #1 and cell #2 shown in Fig. 3*A*, based on small-region analysis

Cell	Path	Distance, μm	Time delay, s	Speed, μm/s
#1 S_d = 30 μm	1 → 4	$d_{14} = 16.7$	$t_4 - t_1 = 0.15$	$d_{14}/(t_4 - t_1) = 111$
	2 → 5	$d_{25} = 16.8$	$t_5 - t_2 = 0.23$	$d_{25}/(t_5 - t_2) = 72.9$
	3 → 6	$d_{36} = 17.2$	$t_6 - t_3 = 0.18$	$d_{36}/(t_6 - t_3) = 95.5$
C_{ICW} (average)				93.2
#2 S_d = 40 μm	1 → 4	$d_{14} = 16.2$	$t_4 - t_1 = 3.55$	$d_{14}/(t_4 - t_1) = 4.56$
	2 → 5	$d_{25} = 16.2$	$t_5 - t_2 = 1.29$	$d_{25}/(t_5 - t_2) = 12.5$
	3 → 6	$d_{36} = 16.2$	$t_6 - t_3 = 1.12$	$d_{36}/(t_6 - t_3) = 14.4$
C_{ICW} (average)				10.5

Table S2. Risetime for 50% peak value of $\Delta[Ca^{2+}]_i$ for all of the small ROI shown in Fig. 6*C*

	Small ROI no.								
	1	2	3	5	6	4	7	9	8
50% risetime, s	4.31	4.40	6.81	7.39	7.56	7.67	8.34	8.91	8.94

Data are organized in the ascending order of the risetime.

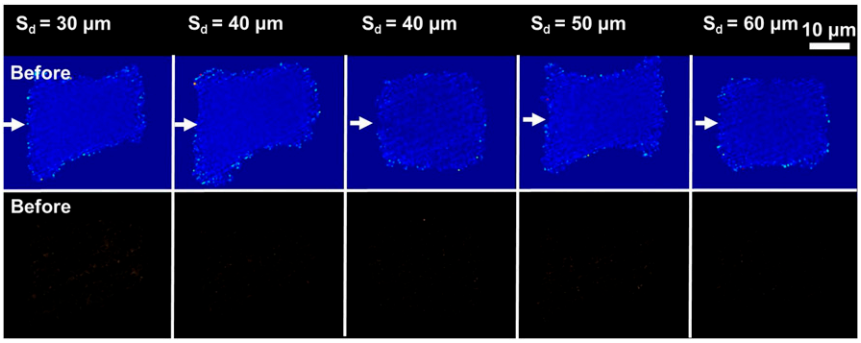

Movie S1. Concurrent intracellular calcium response and PI uptake for representative cells treated at S_d = 30, 40, 50, and 60 μm.

Movie S1

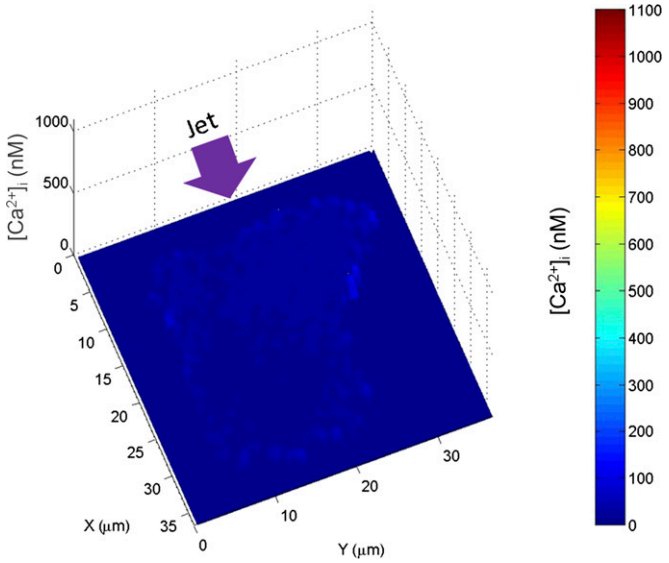

Movie S2. Initiation and propagation of ICW for the cell shown in Fig. 4 with color-coded 3D images: Both the height and color represent the intracellular calcium concentration $[Ca^{2+}]_i$ (nM); the background was subtracted by thresholding, and the cell was stimulated by the jetting flow (denoted by the arrowhead) at $t = 0$.

Movie S2

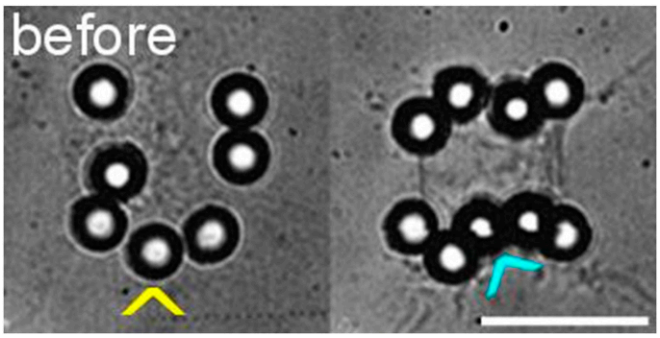

Movie S3. TB interaction with cells attached with 6-μm RGD beads [the response case shown in (*Left*) Fig. 6*A* vs. no response case shown in (*Right*) Fig. 7*A*]. The movie shows the beads displacement and the resultant cellular Ca^{2+} response. (Scale bar, 20 μm.)

Movie S3